Contents lists available at ScienceDirect

European Journal of Radiology Open

Construction of a nomogram combining CEUS and MRI imaging for preoperative diagnosis of microvascular invasion in hepatocellular carcinoma

Feiqian Wang [a,b], Kazushi Numata [b,*], Akihiro Funaoka [b], Takafumi Kumamoto [b], Kazuhisa Takeda [b], Makoto Chuma [b], Akito Nozaki [b], Litao Ruan [a], Shin Maeda [c]

[a] *Ultrasound Department, The First Affiliated Hospital of Xi'an Jiaotong University, No. 277 West Yanta Road, Xi'an, Shaanxi 710061, PR China*
[b] *Gastroenterological Center, Yokohama City University Medical Center, 4-57 Urafune-cho, Minami-ku, Yokohama, Kanagawa 232-0024, Japan*
[c] *Division of Gastroenterology, Yokohama City University Graduate School of Medicine, 3-9 Fukuura, Kanazawa-ku, Yokohama, Kanagawa 236-0004, Japan*

ARTICLE INFO

ABSTRACT

Purpose: To use Sonazoid contrast-enhanced ultrasound (S-CEUS) and Gadolinium-Ethoxybenzyl-Diethylenetriamine Penta-Acetic Acid magnetic-resonance imaging (EOB-MRI), exploring a non-invasive preoperative diagnostic strategy for microvascular invasion (MVI) of hepatocellular carcinoma (HCC).
Methods: 111 newly developed HCC cases were retrospectively collected. Both S-CEUS and EOB-MRI examinations were performed within one month of hepatectomy. The following indicators were investigated: size; vascularity in three phases of S-CEUS; margin, signal intensity, and peritumoral wedge shape in EOB-MRI; tumoral homogeneity, presence and integrity of the tumoral capsule in S-CEUS or EOB-MRI; presence of branching enhancement in S-CEUS; baseline clinical and serological data. The least absolute shrinkage and selection operator regression and multivariate logistic regression analysis were applied to optimize feature selection for the model. A nomogram for MVI was developed and verified by bootstrap resampling.
Results: Of the 16 variables we included, wedge and margin in HBP of EOB-MRI, capsule integrity in AP or HBP/PVP images of EOB-MRI/S-CEUS, and branching enhancement in AP of S-CEUS were identified as independent risk factors for MVI and incorporated into construction of the nomogram. The nomogram achieved an excellent diagnostic efficiency with an area under the curve of 0.8434 for full data training set and 0.7925 for bootstrapping validation set for 500 repetitions. In evaluating the nomogram, Hosmer–Lemeshow test for training set exhibited a good model fit with $P > 0.05$. Decision curve analysis of nomogram model yielded excellent clinical net benefit with a wide range (5–80 % and 85–94 %) of risk threshold.
Conclusions: The MVI Nomogram established in this study may provide a strategy for optimizing the preoperative diagnosis of MVI, which in turn may improve the treatment and prognosis of MVI-related HCC.

1. Introduction

Microvascular invasion (MVI) is recognized as a common risk factor for recurrence after resection of hepatocellular carcinoma (HCC) and is the only or most important risk factor for recurrence [1]. The incidence of MVI in HCC ranged from 15.0 % to 57.1 % [2]. The 3-year recurrence-free survival rate in patients with MVI has decreased from 62.5 % to 27.7 % [3]. It is widely recognized that accurate assessment of MVI is of much importance for HCC clinical decision-making and planning [4]. For example, making a choice between anatomic

hepatectomy and non-anatomical hepatectomy [5], performing a wider surgical margin of more than 1 cm [6], and adding postoperative adjuvant therapy [7].

MVI is defined microscopically as the appearance of endothelial nests of cancer cells surrounding the tumor (predominantly portal vein branches adjacent to the tumor) with no gross tumor macrovascular invasion [8]. Nevertheless, timely and easy diagnosis of MVI is a great challenge for pathologists. The biggest difficulty is that HCC is characterized by significant intratumoral heterogeneity [9], and the current gold standard requires the diagnosis to be taken from surgical resection

[10], which makes it impossible to diagnose MVI before hepatectomy to guide surgical decision-making. Secondly, the pathological diagnosis of MVI require "7-point baseline sampling" [11] and identifies the endothelium and cancer cell location by location. This procedure is tedious and time-consuming in real-world clinical settings. Therefore, the exploration of an easy-to-use strategy for early preoperative diagnosis of MVI is an urgent clinical need to optimize the diagnosis and treatment of HCC.

Contrast-enhanced ultrasound using a Sonazoid (GE Healthcare, Oslo, Norway) agent (S-CEUS) and magnetic resonance imaging with gadolinium-ethoxybenzyl-diethylenetriamine penta-acetic acid (EOB-MRI) have been highlighted as breakthrough imaging modalities for HCC [12] because of their high accuracy, non-radiation, good repeatability, and few side effects [13]. They are particularly suitable for the diagnosis of MVI. Sonazoid for CEUS can more accurately assess the state of the microcirculation taking advantage of its nature of confined to the blood vessels. Contrast-enhanced MRI has better spatial resolution and soft tissue contrast than any other imaging modality, which clearly distinguishes the capsule of the tumor (a frequently studied indicator of MVI) from surrounding tissue [14]. In reality, some imaging features in CEUS and EOB-MRI have been reported to be associated with the occurrence of MVI. A meta-analysis based on 1618 patients and 11 studies revealed that incomplete tumor capsule and nonsmoothed tumor margin determined by US, CT, and MRI would be a risk factor for MVI, with an area under the curve (AUC) of 0.62 and 0.72 for predicting MVI, respectively [15]. Recently, a few researchers established their prediction models for MVI using CEUS [16,17]. Although they have got acceptable or even good diagnostic efficiency with AUC around 0.80, the diagnostic indicators and parameters used in them (such as "ring-like enhancement", "circular enhancement", "unilateral enhancement", "ring thickness grade", "color Doppler flow imaging morphology") are not widely applied in clinical practice, lack of recognized standards and thus there would inevitably be bias from the observers. In addition, some published studies and our previous research consistently found that either S-CEUS or EOB-MRI may be inaccurate and insensitive to the detection of image features of HCC in some cases, such as in deep, ill-defined, heterogeneous, slightly enhanced lesions and pathological early differentiated HCCs [18]. Therefore, it is necessary to apply S-CEUS and EOB-MRI together to accurately diagnose MVI in a multi-modal way, complementing each other's limitations. To the best of our knowledge, few published studies have performed this work [19]. The nomogram model can accurately predict the risk of disease by displaying the corresponding relationship between specific disease and risk factors through an intuitive graphic scoring system [20], which has the overwhelming advantages of individuation and convenient use. There is no doubt that this intuitive, simple, individualized nomogram graphic scoring system is an excellent bridge to apply our research to the real-world clinical practice.

Taken together, by establishing a clinical prediction model combining S-CEUS and EOB-MRI, we wanted to explore an easy-to-use, accurate diagnostic strategy for preoperative diagnosis of MVI in patients with HCC.

2. Materials and methods

2.1. Patient enrollment

From December 2007 to June 2017, 101 patients with 111 HCC lesions were enrolled in this study. The inclusion criteria were as follows: (1) adult patients ($\geq$18 years old); (2) clear pathological diagnosis of HCC; (3) the gold standard of MVI diagnosis can be obtained by surgical histopathology; (4) the lesions were newly discovered and untreated; and (5) patients who underwent both S-CEUS and EOB-MRI examinations within one month before hepatectomy. The exclusion criteria were as follows (Fig. 1): (1) the presence of signs of macrovascular invasion before hepatectomy, such as portal vein invasion or hepatic vein invasion (6 patients); (2) indefinite pathological diagnosis of MVI (one patient); (3) Child-Pugh grade B or C (10 patients); (4) incomplete preoperative clinical and/or serological data (2 patients); (5) poor image quality, which affects the judgment of the imaging indicators involved in this study (one patient), and (6) history of other cancers (10 patents). Clinical information (sex, age, HCC etiology, and existence of cirrhosis),
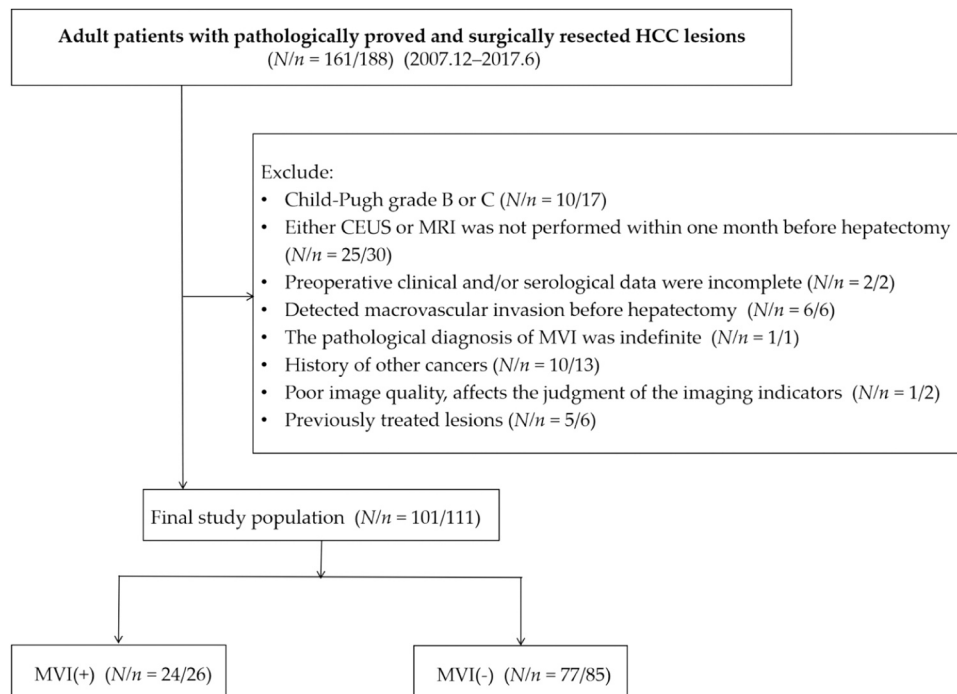

Fig. 1. Flowchart of the study population. HCC: hepatocellular carcinoma; MVI: microvascular invasion; S-CEUS: Sonazoid contrast-enhanced ultrasound; EOB-MRI: Gadolinium-Ethoxybenzyl-Diethylenetriamine Penta-Acetic Acid magnetic-resonance imaging. "N" represent "the number of patients" while "n" represent "the number of lesions".

preoperative serological indicators (including alpha-fetoprotein (AFP), serum albumin (Alb), total bilirubin (T-BIL), platelets (Plt), prothrombin time-international normalized ratio (PT-INR) (prothrombin induced by vitamin K absence II (PIVKA-II), and indocyanine green 15 min retention (ICG-R15)), imaging data, and pathological reports of HCC and MVI were retrospectively collected from a review of the electronic medical record system, radiology database, and pathology records from our hospital. We used 200 ng/mL as cut-off value for AFP levels at baseline, as suggested by the Asia Pacific Association for the Study of the Liver HCC guideline [21]. Data collection and analysis were approved by the Ethics Review Board (No. F220700009 on June 27, 2022) of Yokohama City University Medical Center of Japan. The requirement for informed consent was waived because of the retrospective nature of the study.

All of the 111 lesions were used to construct the training set (full data training set), and then the method of "bootstrap using computer resampling for 500 repetitions" was used on these 111 lesions for invalidating the performance of our model.

2.2. Grayscale US and S-CEUS examination

A LOGIQ E9 US system (GE Healthcare, Milwaukee, WI, USA) equipped with native tissue harmonic grayscale imaging and CEUS function was used. Convex and microconvex with frequencies of 1–6 MHz and 2–5 MHz, respectively, were used.

First, grayscale US was performed. The size (largest axial diameter on the images) and location of the lesion were recorded. Subsequently, a 0.2 mL dose of Sonazoid was injected into the antecubital vein at 0.2 mL/s via a 24-gauge cannula, followed by 2 mL of 5 % glucose. CEUS images were acquired during three contrast phases: an arterial phase (AP), portal phase (PP), and post-vascular phase (PVP) (10–50 and 80–120 s, and 10 min after injection, respectively). If the lesion was indistinct (especially if it was isoechogenic) on the grayscale US image, size measurement on the AP or PVP of the CEUS images could be performed instead [22].

2.3. EOB-MRI examination

MR was performed using a 1.5 T whole-body imager (Avant; Siemens Medical Systems, Erlangen, Germany). A power injector (Spectris Solaris EP; MEDRAD, Bayer Schering Pharma AG, Berlin, Germany) was used to inject 0.1 mmol/kg of Gd-EOB-DTPA (Primovist; Bayer Schering Pharma AG, Berlin, Germany) at 1 mL/s through a catheter placed in the antecubital vein, followed by flushing with 20 mL of sterile saline solution at 2 mL/s. AP, PP, late-phase, and hepatobiliary phase (HBP) scanning was performed at 25–30 s, 70–85 s, 180 s, and 20 min after initiation of the contrast injection, respectively. Images were obtained using fat-suppressed volumetric interpolated breath-hold examination (FS VIBE) T1-weighted sequences (TR, 6.2 ms; TE, 3.15 ms; flip angle, 20º; bandwidth, 260 Hz/pix; matrix, 166 × 320; acquisition time, 20 s). In addition, a fast low-angle shot (FLASH) T1-weighted sequence (TR, 115 ms; TE, 4.76 ms; flip angle, 70º; bandwidth, 260 Hz/pix; matrix, 192 × 256; acquisition time, 20 s × 3) was performed.

2.4. Interpretation of key imaging features

There were 12 imaging features included in this study. They were as follows. 1) size (≤/> 53.5 mm); 2) tumoral capsule in S-CEUS or EOB-MRI (presence/absence); 3) the integrity of tumoral capsule in S-CEUS or EOB-MRI (complete/incomplete); 4) AP enhancement degree in S-CEUS (hyper-/iso-enhancement); 5) PP enhancement degree in CEUS (iso-/hypo-enhancement); 6) PVP enhancement degree in S-CEUS (iso-/hypo-enhancement); 7) homogeneity in AP of S-CEUS (homogeneity/heterogeneity); 8) homogeneity in HBP of MRI (homogeneity/heterogeneity); 9) margin in HBP of EOB-MRI(regular/irregular); 10) signal intensity in HBP of MRI (low/others); 11) peritumoral wedge-shape enhancement in HBP of MRI (presence/absence); 12) intratumoral

branching enhancement in AP of S-CEUS (presence/absence). Two doctors (F. W. and A.F., with 11 and 5 years of experience in abdominal imaging diagnosis, respectively) independently evaluated the image features of S-CEUS and EOB-MRI, respectively, without knowing the patients' clinical, laboratory, or imaging information or their gold-standard MVI diagnosis results. When there were inconsistent results between the two doctors after the first image analysis, a final decision was made by an expert (K. N., with 35 years of experience in liver imaging diagnosis). If either EOB-MRI or S-CEUS detects the appearance of "peritumoral wedge shape", "presence and incomplete tumoral capsule", and "presence of branching enhancement", these image features are considered to be present. The imaging features are defined as follows (Table 1 and Fig. 2).

Table 1
The definition of key image features used in our study[1].

Image Features	Imaging modes/ phases	Definition
Size	Any phase in US or MRI images	Clearly displayed largest axial diameter
Hypervascularity	Any phase in S-CEUS	There were more perfusion of contrast agent in the lesion than in the surrounding liver parenchyma, regardless of the proportion of hypervascular area.
Hypovascularity	Any phase in S-CEUS	No definite hypervascularity was shown in any area of the lesion. In addition, there were less perfusion of contrast agent in the lesion than in the surrounding liver parenchyma, regardless of the proportion of hypovascular area.
Isovascularity	Any phase in S-CEUS	Enhancement was questionable, or the degree of lesion enhancement was the same as that of the surrounding liver parenchyma.
Homogeneity/ heterogeneity	AP of S-CEUS/ HBP of EOB-MRI	Regarding the internal homogeneity of the contrast agent distribution, homogeneous enhancement was defined as a whole and diffuse enhancement of the lesion, while heterogeneous enhancement was defined as two or more enhancement echoes mixed enhancement of the lesion.
Tumor capsule[2]	AP or HBP/PVP of EOB-MRI/S-CEUS	Thin ring-like enhancement surrounding the tumor (which was different from that of the lesion or surrounding tissue)
Incomplete capsule[2]	AP or HBP/PVP of EOB-MRI/S-CEUS	Certain area of capsule is disrupted or even disappear
Tumor margin[2]	HBP of EOB-MRI	The interface between the tumor and the normal liver tissue
Irregular margin[2]	HBP of EOB-MRI	"Irregular" margin is uneven, coarse, ill-defined, indistinct rather than smooth; lobulated rather than round
Peritumoral wedge Shape	HBP of EOB-MRI	Peritumoral parenchymal enhancement with a wedge-shaped or bud-shaped protrude
Branching enhancement	AP of S-CEUS	Thick or thin continuous strip-like, branching, separation-like enhancement

[1] MVI: microvascular invasion; HCC: hepatocellular carcinoma; US: ultrasound; CEUS: contrast-enhanced ultrasound; S-CEUS: CEUS performed using contrast agent Sonazoid; AP: arterial phase; PVP: postvascular phase; MRI: magnetic resonance imaging; HBP: hepatobiliary phase; EOB-MRI: Gadolinium-Ethoxybenzyl-Diethylenetriamine Penta-Acetic Acid magnetic resonance imaging.
[2] For the indicator that can be obtained by two imaging modalities (S-CEUS, EOB-MRI), positive is determined as long as either modality detects a positive imaging appearance.
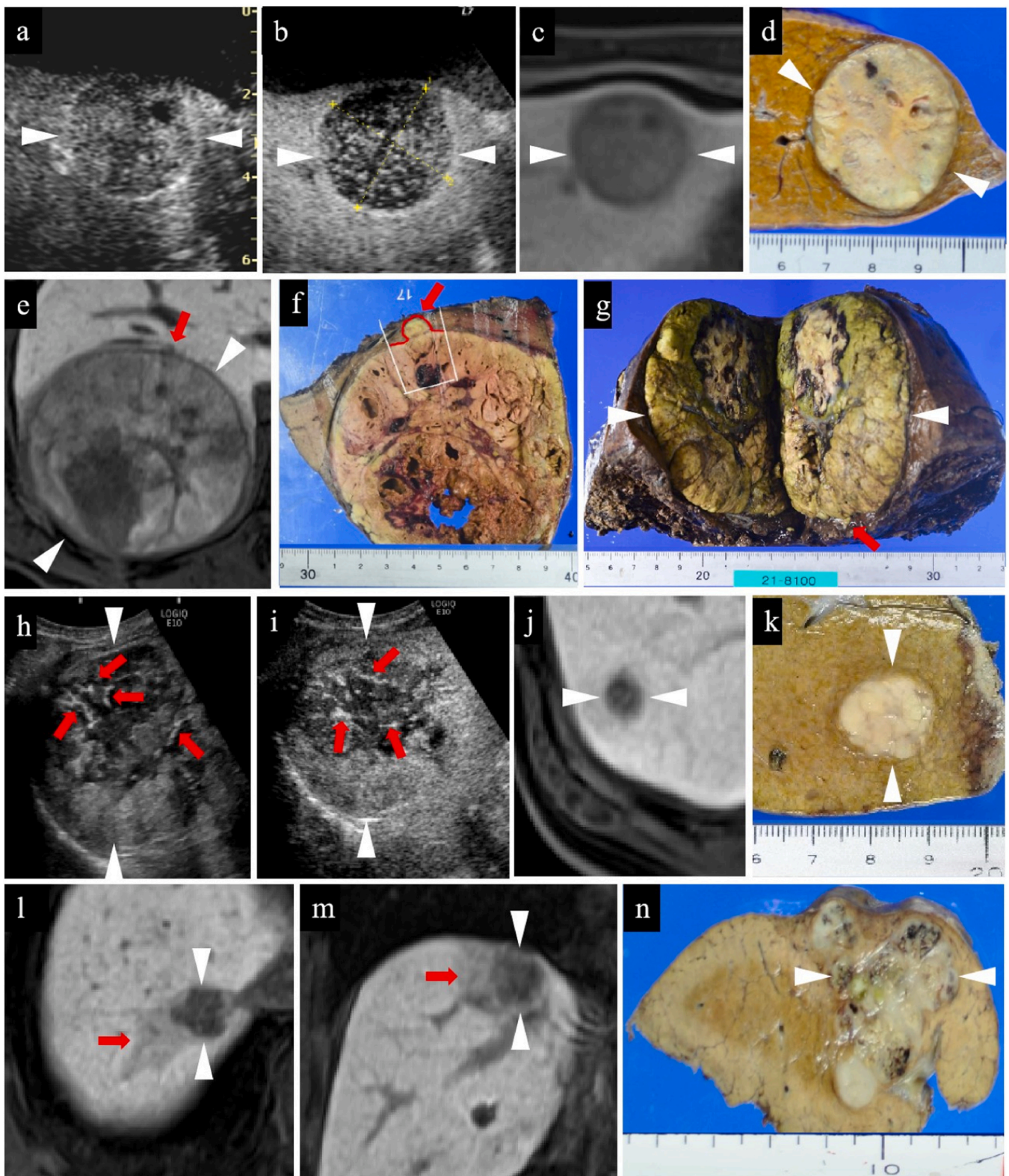
Fig. 2. Typical imaging features from our four cases. (a–d) are case 1 showing a lesion with regular margin (round) and complete capsule. (a) is AP while (b) is PVP of S-CEUS, (c) is HBP of EOB-MRI. (e–i) are case 2. The red arrow in (e–g) point to the small disrupt area on the capsule. (e–g) exhibit the incomplete capsule while (h–i) the branching enhancement in AP of S-CEUS. (h) is the image at the first time of the injection of Sonazoid agent while (i) is at re-injection. The red arrows in (h–i) indicate the branching enhancement area. (j–k) are case 3. (j), which is HBP of EOB-MRI, shows the lesion with no capsule surrounding the tumor while (k) shows no capsule in gross specimen. (l–n) are case 4. (l–n) show irregular margin (lobulated) and peritumoral enhancement with a wedge shape in HBP of EOB-MRI (l–m, red arrows). The white arrowheads in all the figures refer to the location of lesions. (d, f, g, k, n) are the cut surface of gross resected specimen of HCC lesions and surrounding area.

2.5. Histopathological evaluation of MVI

In this study, the gold-standard diagnosis of MVI was achieved using surgical resection and microscopic diagnosis. Open or laparoscopic resection was performed. Fresh surgical specimens, including para-cancerous (less than 1 cm to cancer) and distal cancerous (approximately 5 cm to cancer) tissues, were obtained from all the enrolled lesions. All tissues were fixed in 10 % neutral formalin, embedded in paraffin, and cut into 4 μm-thick sections. For the diagnosis of MVI, the sections were stained with hematoxylin-eosin (HE) and observed under a light microscope. When it was difficult to make a definite diagnosis with HE staining, immunohistochemical analysis of elastin van Gieson (EVG) staining was performed to assist in the diagnosis of MVI.

2.6. Statistical analysis

The enumeration data of baseline clinical and serological characteristics between MVI-positive and MVI-negative groups were calculated using the chi-squared test. Continuous variables that showed normal distribution (patient age and Alb) were presented as mean ± standard deviation and compared using the Student's t test. Non-normally distributed data (T-BIL, PT-INR, Plt, and ICG-R15) were presented as medians and quartiles, and the Mann–Whitney U-test was used to compare intergroup differences. In the training set, the least absolute shrinkage and selection operator (LASSO) logistic regression analysis and afterwards multivariate analysis were used to screen the independent risk factors and build a prediction nomogram for the diagnosis of MVI. The performance of the nomogram was evaluated using the receiver operating characteristic (ROC) curve, decision curve analysis (DCA) and calibration curve. ROC analysis and DCA were again performed in internal bootstrap validation. The differences of ROC between training set and internal bootstrap validation were compared using the Delong test. The inter-observer variability for radiological features was assessed using the Kappa analysis (κ=0.00–0.20, poor agreement; κ=0.21–0.40, fair agreement; κ=0.41–0.60, moderate agreement;

κ=0.61–0.80, good agreement; κ=0.81–1.0, excellent agreement). All statistical analyses were performed using STATA 15.0, R 4.0.3 and MedCalc. Statistical significance was set $P < 0.05$.

3. Results

3.1. Baseline characteristics

The 111 lesions included 85 MVI-negative and 26 MVI-positive lesions. The incidence of MVI was 23.42 %. The cutoff value of PIVKA-II (40 mAU/mL) and size (53.5 mm) was determined by the Youden's index obtaining from ROC curve analysis. The baseline patient characteristics were depicted in Table 2. In addition to Plt and PIVKA-II, there were no statistical differences in the clinical or serological indicators between the MVI-positive and MVI-negative groups.

3.2. Selection of risk factors of MVI

The inter-observer agreement between the two doctors (F. W. and A. F.) was high using radiological features to predict MVI. The level of agreement for "branching enhancement", "integrity of capsule", "wedge" and "signal intensity in HBP of MRI" was good (kappa: 0.61–0.80), while the agreement for all the other imaging features was excellent (kappa: 0.81–1.0).

To prevent overfitting of the variables and to simplify the model, LASSO regression analysis was used to penalize the absolute value of the coefficients. We included all the 12 imaging features, two baseline characteristics that were statistically different between the MVI-positive and-negative groups (Plt and PIVKA-II in Table 2), and two MVI-related indicators mentioned in the literature (AFP [23] and presence of cirrhosis [24]) for LASSO regression analyses. The results of the LASSO regression revealed the following eight variables as risk factors affecting the development of MVI in HCC patients. They were "peritumoral wedge", "margin", "signal intensity in HBP", "integrity of capsule", "branching enhancement in S-CEUS", "size with cutoff value of

Table 2
Baseline characteristics of the study population[1,2].

	All patients n=101	MVI-positive $n = 24$	MVI-negative $n = 77$	t/χ^2/U value	P value[3]
Clinical characteristics					
Age ($\bar{x} \pm s$, years)	67.59±9.883	64.96±11.984	68.42±9.066	1.506	0.135
Gender (No. (%))				0.536	0.464
Male	81 (80.2)	18 (75.0)	63 (81.8)		
Female	20 (19.8)	6 (25.0)	14 (18.2)		
Etiology (No. (%))				6.546	0.294
HCV and/or HBV	58 (57.4)	16 (66.7)	42 (54.5)		
Others[3]	43 (42.6)	8 (33.3)	35 (45.5)		
Presence of cirrhosis (No. (%))				0.091	0.763
Yes	49 (48.5)	11 (45.8)	38 (49.4)		
No	52 (51.5)	13 (54.2)	39 (50.6)		
Serological characteristics					
AFP (No. (%))				2.465	0.116
≤200 ng/mL	79 (78.2)	16 (66.7)	63 (81.8)		
>200 ng/mL	22 (21.8)	8 (33.3)	14 (18.2)		
Alb [M (Q1, Q3), g/dL]	4.18±0.506	4.21±0.638	4.17±0.498	0.366	0.715
T-BIL [M (Q1, Q3), mg/dL]	0.900 (0.700, 1.100)	0.850 (0.625, 1.100)	0.900 (0.700, 1.100)	827.5	0.680
PT-INR [M (Q1, Q3)]	1.040 (0.970, 1.040)	1.020 (0.963, 1.125)	1.040 (0.975, 1.120)	846.5	0.536
Platelets [M (Q1, Q3), ×10^{10}/L]	15.400 (10.550, 20.000)	19.350 (13.375, 21.975)	14.800 (10.000, 19.850)	657.5	0.043
PIVKA-II (No. (%))				6.314	0.012
≤40 mAU/mL	34 (33.7)	3 (12.5)	31 (40.3)		
>40 mAU/mL	67 (66.3)	21 (87.5)	46 (59.7)		
ICG-R15 [M (Q1, Q3),%)]	15.150 (9.785, 22.160)	14.475 (9.848, 21.795)	15.255 (9.733, 22.800)	859.0	0.669

[1] Abbreviations: HCC, Hepatocellular carcinoma; HCV, hepatitis C virus; HBV, hepatitis B virus. AFP, alpha-fetoprotein; Alb, serum albumin; T-BIL, total bilirubin; PT, prothrombin time;; INR, international normalized ratio; PIVKA-II, prothrombin induced by vitamin K absence II; ICG-R15:Indocyanine green 15 min retention; MVI, microvascular invasion. $\bar{x} \pm s$: Mean±standard deviation; M(Q1,Q3): median (1st quartile, 4th quartile).

[2] The groupings of MVI and statistics in this table are based on patients.

[3] "Others" included etiologies of alcoholic liver disease, non-HBV non-HCV, nonalcoholic steatohepatitis, and primary biliary cirrhosis.

53.5 mm", "PIVKA-II with cutoff value of 40 mAU/mL", and "AFP with cutoff value of 200 ng/mL" (Fig. 3).

We put these eight variables into multivariate analysis. By stepwise regression, models with smaller degree of freedom (DF) and Akaike Information Criterion (AIC) were selected (DF = 5, AIC = 94.302) (Table 3). In the end, only four variables (margin, peritumoral wedge, and integrity of capsule, branching enhancement) with *P* less than 0.05 were selected for final prediction model.

3.3. Development of the MVI-predicting nomogram

Incorporating four indicators of "branching enhancement", "peritumoral wedge", "margin", and "integrity of capsule", an MVI risk nomogram was developed and was presented in Fig. 4. Take an example to explain the nomogram model, if an HCC lesion has peritumoral wedge (approximately equal to 100 points), irregular margin (77.5 points), incomplete capsule (86 points), but no branching enhancement in CEUS (0 points), the total points is 263.5, the corresponding probability of MVI is estimated to be 78 %.

3.4. Evaluation of the MVI-predicting nomogram

3.4.1. The calibration and net benefit gain for the nomogram

The Hosmer-Lemeshow (H-L) test was used to evaluate the goodness-of-fit of the logistic regression model. The results of H-L test for training set were that $\chi^2 = 2.4719$, df = 5, P = 0.7807. Seen from Fig. 5(a), at a probability of 0.38–0.7, the training set-derived curve (blue line) may slightly overestimate the risk of MVI, while at the rest area of predicted probability, the model may exactly predict the probability. Bootstrap validation-derived curve (red line) demonstrated that at a probability of 0–0.5, the model may overestimate the risk of MVI, while when the probability was higher than 0.5, the model may underestimate the probability. Both two lines fits well with the ideal line (dotted line). All the above results showed that the model was of excellent goodness-of-fit. Fig. 5(b) showed the DCA. It revealed that the net benefit rate was >0 when at a risk threshold is 5–80 % and 85–94 %. Moreover, within this range, the smaller the threshold, the higher the net benefit rate. A wide range may suggest that using this nomogram to predict MVI added more benefits for clinical use than either the predict-all-lesions as MVI or the predict-none-lesions as MVI. For internal bootstrap validation, the risk threshold probability also has a wide range (approximately 8–80 % and 92–99 %).

3.4.2. The discrimination of the training set and validation set

The AUC of our model was 0.8434 (95 % confidence interval [CI]: 0.7516–0.9353). Sensitivity and specificity were 0.346 and 0.977, respectively. For internal bootstrap validation, accuracy was slightly lower. Although the AUC of the full data training set and internal bootstrap validation set was statistically different by Delong test (*P*=0.0007), the AUC value of 0.793 for internal bootstrap validation suggested that the good predictive accuracy of the model was preserved (Table 4).

Seen from Supplementary Figure 1c, our model pooling the four imaging features had a higher AUC than independently using the four imaging features diagnosing MVI, suggesting that a combined application of EOB-MRI and CEUS could achieve synergistic effects in the diagnosis of MVI and improve diagnostic ability. Seen from Supplementary Figure 1d, the area under the Precision-Recall (PR) curve was greater than 0.5. All these results suggested that our final model has good discrimination and diagnostic efficacy. In summary, from all aspects, the model we built has achieved good efficiency (Supplementary Table 1).

4. Discussion

Our results confirmed that some imaging features are associated with MVI. More important, MVI can be predicted by combining a few key imaging features. S-CEUS and EOB-MRI can detect the change in hemodynamics in microvascular system sensitively. By reviewing a large body of relevant literature on the mechanisms by which MVI occurs and how these imaging features are generated, we can reasonably explain our findings from the perspective of radiological/pathological correlation.

"Intratumoral branching enhancement" is a factor that entered our model. Branching enhancement were detectable only in the AP of S-CEUS, strongly suggesting branching enhancement as arteries. Many researchers believe that when HCC and even MVI develop, emboli form in the hepatic veins and portal venous system, leading to the reduction or even stoppage of venous flow. This occlusion could possibly stimulate a compensatory increase (maybe both in density and volume) of the intratumoral feeding arteries [25], which is visually reflected as "intratumoral branching enhancement" in the AP of S-CEUS imaging. Accordingly, a large number of new microvessels that proliferate in the tumor further aggravates MVI. This is because these microvessels are quite different from the normal vessels. They are immature, structurally
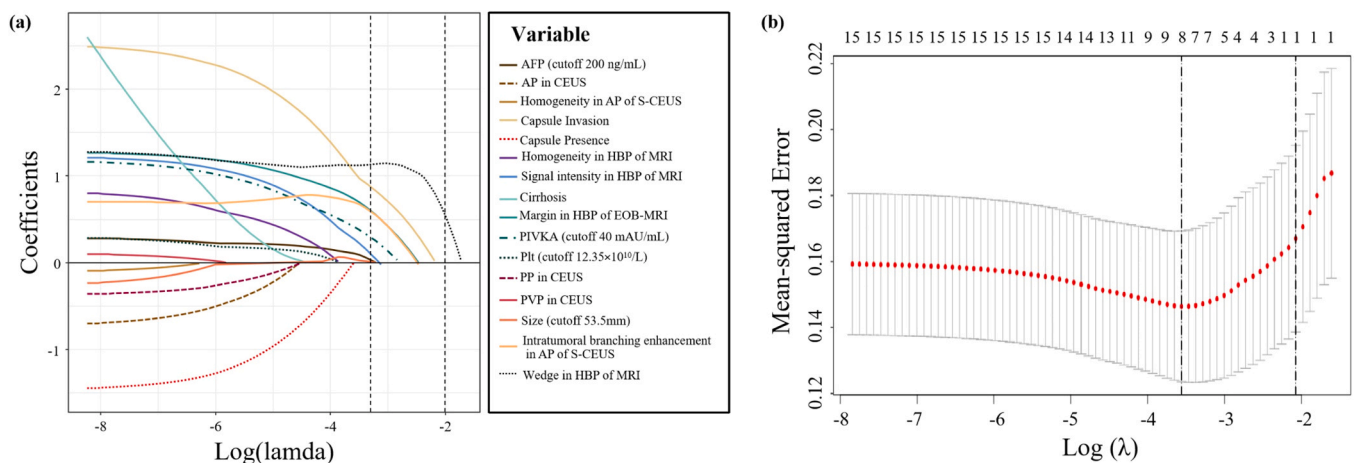

Fig. 3. Features selection using the LASSO binary logistic regression model. (a) Log (Lambda) value of the 16 features in the LASSO model. A coefficient profile plot was produced against the log (lambda) sequence. (b) Variable selection in the LASSO model used 10-fold cross-validation via minimum criterion. Partial likelihood deviation (binomial deviation) curves and logarithmic (lambda) curves were plotted. Use the minimum standard and 1se (1-SE standard) of the minimum standard to draw a vertical dashed line at the optimal value. The optimal lambda produced 8 nonzero coefficient variables. Abbreviations: LASSO, least absolute shrinkage and selection operator; SE, standard error.

Table 3
Final predictors for the risk of MVI in HCC patients[1].

Characteristics	β	SE	OR	95 %CI	Z	P
(Intercept)	-3.58	0.72116	0.028	0.027 (0.005–0.096)	-4.964	<0.001
Peritumoral wedge	2.011	0.59965	7.471	7.471 (2.365–25.46)	3.354	0.001
Margin	1.414	0.63829	4.113	4.113 (1.240–15.76)	2.216	0.027
Integrity of capsule	1.5	0.58096	4.483	4.482 (1.489–14.97)	2.582	0.01
Branching enhancement	1.493	0.74239	4.451	4.451 (1.043–20.11)	2.011	0.044

[1] Abbreviations: HCC, Hepatocellular carcinoma; MVI, microvascular invasion; SE, standard error; OR, odds ratio; CI, confidence intervals.
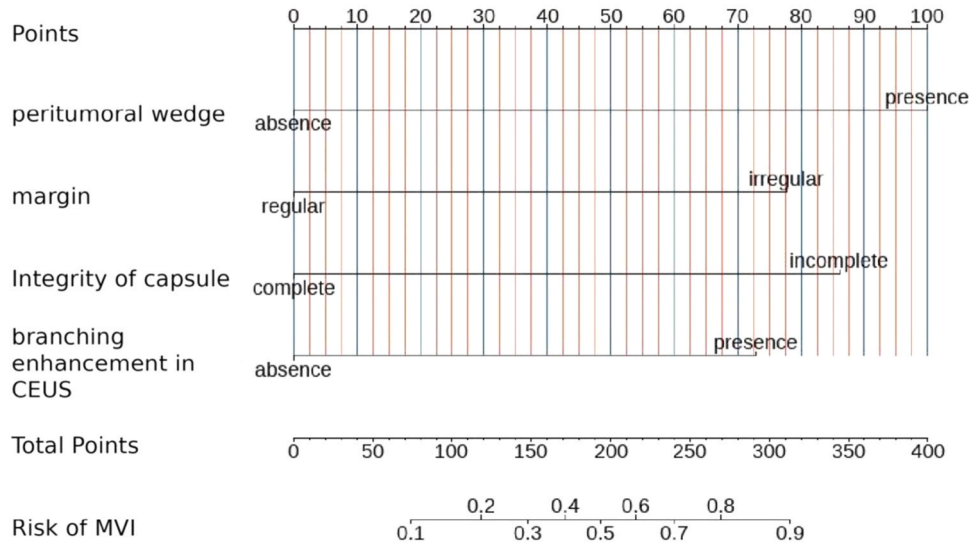

Fig. 4. Nomogram prediction model for MVI. Abbreviations: CEUS, contrast-enhanced ultrasound; MVI, microvascular invasion.
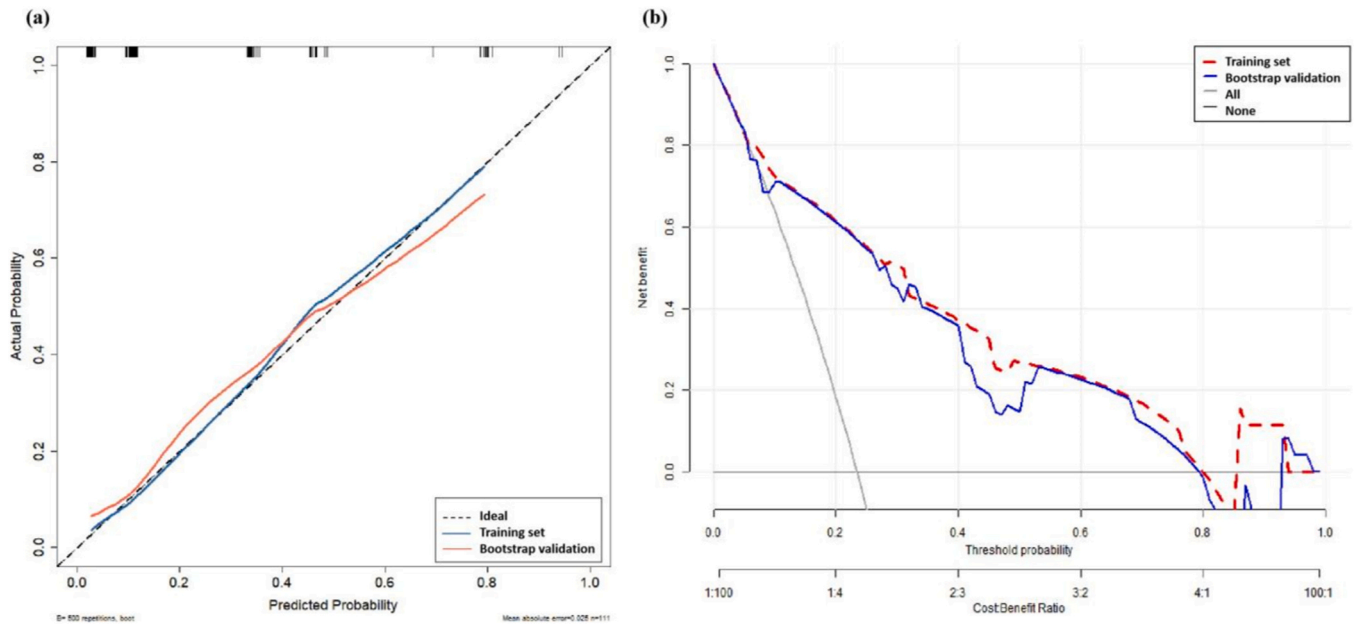

Fig. 5. Calibration curve (a) and Decision curve analysis (b) for the nomogram. (a)The blue line represents the full data training set while the red line bootstrapping for 500 repetitions. (b)The dotted red line represents the training set while blue line internal bootstrap validation set.

incomplete, and exhibit increased permeability [26]. These characteristics would facilitate the entry of large numbers of cancer cells into the microvessels, thereby promoting MVI. That is why "intratumoral branching enhancement" occurs and why it is related to MVI development (Complement each other and promote each other).

"The integrity of tumor capsule" rather than "the presence of tumor capsule" entered our prediction model of MVI. According to previous studies, HCC lesions with a true fibrous capsule or even pseudocapsule are considered favorable prognostic factors because the capsule temporarily acts as a physical barrier to block cancer cells from dissemination [27]. Therefore, some studies have attempted to use images to detect capsules and predict MVI. However, the relationship

Table 4
The discrimination between the training set and the validation set[1].

	Sensitivity	Specificity	PPV	NPV	Accuracy	AUC	*P*
Full data training set	34.62 %	97.65 %	81.82 %	83.00 %	82.88 %	0.8434	0.0007
Bootstrap validation set	38.46 %	94.12 %	66.67 %	83.33 %	81.08 %	0.7925	

[1] Abbreviations: PPV, Positive predictive value; NPV, Negative predictive value; AUC, area under the curve.

between the radiologic tumor capsule and MVI has been positive, negative, inconclusive, or controversial in different studies [17,28,29]. To dig the reason deeper from pathological perspective, "absence"–"presence of complete capsule"–"presence of incomplete capsule" might be step-wise distinct (or sometimes may overlapping) stages of the carcinogenesis. In the early stages, tumor cells are well differentiated and exhibit relatively benign slow growth. The lesion did not form a capsule or a defined fibrous capsule. Over time, lesions that acquired malignant potential showed an expansive growth pattern. The lesion mechanically pushed the surrounding tissue to form a pseudocapsule. At this stage, the tumors maintained their liver cell-plate morphology. At the final stage, the progressed HCC lesion showed an infiltrative histological growth pattern [30]. Cancerous cells penetrate, rupture, or even destroy the capsule (which appears in the images as an incomplete capsule) and replace the peritumoral parenchymal tissue; hence, MVI develops. That is the reason why the presence of an incomplete capsule rather than the presence of a capsule is related to MVI.

"Peritumoral wedge enhancement" was a critical imaging feature of our prediction model as the odds ratio (suggesting the importance of the variable contribution to the model) of 7.471 was much greater than the other four imaging features (Table 3). It should be noted that the characteristic imaging findings of "peritumoral" and "intratumoral" are different. To be specific, "peritumoral wedge enhancement in EOB-MRI" occurs in a "region". It did not show the fine structure of the vascular tree as our other indicator "intratumoral branching enhancement in S-CEUS". The mechanisms of "peritumoral wedge enhancement" is that tumor cells invade both peritumoral proliferating microvessels and the peritumoral stroma. Regarding microvessels, during the progression of MVI, the peritumoral area forms ill-structured neovascularization as changes within the tumor. In terms of stroma, as described above, intratumoral tumor cells destroy the tumor capsule and invade the surrounding parenchymal tissues by a replacement (rather than pushing out) growth pattern. Enhancement in "one area" is undoubtedly easier to identify than enhancement in fine "branching". However, this imaging feature is not necessarily an MVI; it may also be an invasion of peritumoral stroma.

The fourth imaging feature entered the prediction model was "irregular margin". In agreement with our findings, "irregular margin" was reported to be frequently present in MVI-positive lesions than in MVI-negative lesions [31]. A recent study conducted by Wang et al. demonstrated that the tumor margin evaluated on MRI reflects the pathological characteristics of the gross appearance [32]. Pathologically, gross HCC lesions of "nodular with extranodular growth type" and "multinodular confluent type" would show irregular tumor margins on MRI [32]. These gross patterns showed a higher risk of MVI, more stemness features, and poorer prognosis than "single nodular growth type" [33].

Five imaging features ("intratumoral heterogeneity in AP of CEUS and HBP of EOB-MRI" and "intratumoral enhancement degree in AP, PP, PVP of CEUS") were included in the statistical analysis initially as possible risk factors for MVI. Unfortunately, however, they were not included in the final prediction model after LASSO regression analysis and multivariate regression analysis.

"Intratumoral heterogeneity" is frequently described in MVI studies. We observed in both EOB-MRI and S-CEUS examinations in our study. The features of intratumoral heterogeneity were identified as unrelated to MVI. The two typical manifestations of heterogeneity (mosaic architecture and nodule-in-nodule architecture) may have opposite effects on

MVI. Mosaic architecture is believed to be caused by complex tissue composition, including but not limited to fat deposition, necrosis, and hemorrhage. Mosaic architecture has been reported to be an independent risk factor for MVI (odds ratio, 3.420; $P < 0.001$); however, there is insufficient explanation [34]. Nodule-in-nodule architecture was reported to be an independent protective predictor of MVI [35]. The explanation is that the "nodule-in-nodule architecture" is the appearance of a mixed histologically differentiated composition of cancer cells. The inner nodule shows characteristics of a progressed HCC, whereas the outer nodule manifests characteristics of an early HCC or a dysplastic nodule that is less aggressive.

"Intratumoral enhancement degree" in three phases of S-CEUS were observed in our study. When MVI occurs, a large number of arteriovenous short circuits are more likely to form, resulting in a fast clearance of the contrast agent. As reflected in the S-CEUS parameters, the washout time is significantly shortened [36]. Based on this theory, some studies have found that hypovascularity in PP and hypoechogenicity in PVP can differentiate between MVI-positive and MVI-negative groups [36,37]. Unfortunately, other studies [17] and our study failed to find any relationship between tumoral enhancement in any of the three S-CEUS phases and the presence of MVI. This discrepancy may be attributed to the heterogeneity of the study population or unknown reasons.

Our final prediction model of MVI incorporated both intratumoral (intratumoral branching enhancement) and peritumoral (peritumoral wedge) imaging features. Early research on MVI has focused on intratumoral changes. In recent years, an increasing number of researchers have begun to explore changes around tumors. Theoretically, liver cancer is recognized as an entire ecosystem in which tumor cells cooperate with host cells in their intratumoral and peritumoral microenvironment [38]. In agreement, it was reported that the MVI radiomics models based on combined intratumoral and peritumoral data yielded better results than those based solely on intratumoral and peritumoral data [39]. Thus, although MVI is observed microscopically outside the tumor, our model may suggest that both the intratumoral and peritumoral factors should be considered in MVI studies.

Our study had several limitations. First, this was a retrospective study, with all the limitations derived from this. Second, we analyzed only the imaging indicators routinely used for clinical diagnostic purposes; therefore, other prognostic markers frequently analyzed in experimental settings, for example, quantitatively analysis of "time to peak" and "peak intensity of contrast agent" by time-intensity curve, were not involved in this study. Third, cases were collected over a period of 10 years, from 2007 to 2017. Such a long time would possibly have the renewal of instruments, updating of equipment, and the advancement of imaging diagnostic technology. Fourth, owing to the small sample size of this study (111 lesions), we did not split the samples into development and validation. We validated by resampling of original datasets (that is type 1b of the six types of prediction model [40]). Fourthly, HCC in Japan is characterized by histological early stage, small size liver cancer, and hepatitis C as the etiology, therefore, our nomogram can not be applied to the liver cancer population in the other area of the world with different characteristics. The plan of our future research is to collect China-Japan multi-center, large-sample liver cancer data and build clinical prediction model which include both training set and external validation set. We hope that our advanced clinical prediction model will have higher accuracy and better generalizability due to its completeness and rigor. Finally, we converted some continuous variables (e.g., PIVKA-II, AFP, and size) into categorical variables

using an optimal cut-off value when performing LASSO regression analysis for building prediction model. The drawback is that statistical power would be reduced; therefore, the true relationship between some variables and the occurrence of MVI might be underestimated or hidden because of the potential information loss of variables [41]. This might also be the reason why Plt yielded a statistical difference between the MVI-positive and MVI-negative groups as a continuous variable ($P = 0.043$) but failed to be selected into our final prediction model. Nonetheless, despite these limitations, this is the first prediction model to combine a few clinically available indicators of CEUS and enhanced-contrast MRI to diagnose MVI.

5. Conclusion

Based on the features of CEUS and EOB-MRI, we successfully established a clinical prediction model of MVI with high accurancy and professionally presented it with a visualized nomogram. Our nomogram aiming to preoperatively, non-invasively and accurately diagnosis MVI might provide a way for MVI-related treatment and prognosis of HCC.

CRediT authorship contribution statement

Akito Nozaki: Data curation. **Makoto Chuma:** Methodology. **Kazuhisa Takeda:** Writing – review & editing. **Shin Maeda:** Supervision. **Litao Ruan:** Writing – original draft. **Takafumi Kumamoto:** Formal analysis. **Akihiro Funaoka:** Investigation. **Kazushi Numata:** Conceptualization. **Feiqian Wang:** Funding acquisition.

Declaration of Competing Interest

The authors declare that they have no known competing financial interests or personal relationships that could have appeared to influence the work reported in this paper.

Data Availability

The data presented in this study are available from the corresponding authors upon request. The data were not publicly available because of privacy concerns.

Conflict of Interest

The authors declare that the research was conducted in the absence of any commercial or financial relationships that could be construed as potential conflicts of interest.

Institutional review board statement

This study was approved by the Yokohama City University Medical Center Institutional Review Board (no. F220700009) on June 27, 2022, and was conducted in accordance with the Declaration of Helsinki on good clinical practice.

Appendix A. Supporting information

Supplementary data associated with this article can be found in the online version at doi:10.1016/j.ejro.2024.100587.

References

[1] P.R. Tung-Ping, S.T. Fan, J. Wong, Risk factors, prevention, and management of postoperative recurrence after resection of hepatocellular carcinoma, Ann. Surg. 232 (2000) 10–24, https://doi.org/10.1097/00000658-200007000-00003.

[2] J.C. Lee, H.C. Hung, Y.C. Wang, C.H. Cheng, T.H. Wu, C.F. Lee, T.J. Wu, H.S. Chou, K.M. Chan, W.C. Lee, Risk score model for microvascular invasion in hepatocellular carcinoma: the role of tumor burden and alpha-fetoprotein, Cancers (Basel) (2021) 13, https://doi.org/10.3390/cancers13174403.

[3] S. Sumie, O. Nakashima, K. Okuda, R. Kuromatsu, A. Kawaguchi, M. Nakano, M. Satani, S. Yamada, S. Okamura, M. Hori, et al., The significance of classifying microvascular invasion in patients with hepatocellular carcinoma, Ann. Surg. Oncol. 21 (2014) 1002–1009, https://doi.org/10.1245/s10434-013-3376-9.

[4] H.T. Hu, Z. Wang, M. Kuang, W. Wang, Need for normalization: the non-standard reference standard for microvascular invasion diagnosis in hepatocellular carcinoma, World J. Surg. Oncol. 16 (2018) 50, https://doi.org/10.1186/s12957-018-1347-0.

[5] X.P. Zhong, Y.F. Zhang, J. Mei, S.H. Li, A. Kan, L.H. Lu, M.S. Chen, W. Wei, R. P. Guo, Anatomical versus non-anatomical resection for hepatocellular carcinoma with microscope vascular invasion: a propensity score matching analysis, J. Cancer 10 (2019) 3950–3957, https://doi.org/10.7150/jca.32592.

[6] W. Wang, Y. Guo, J. Zhong, Q. Wang, X. Wang, H. Wei, J. Li, P. Xiu, The clinical significance of microvascular invasion in the surgical planning and postoperative sequential treatment in hepatocellular carcinoma, Sci. Rep. 11 (2021) 2415, https://doi.org/10.1038/s41598-021-82058-x.

[7] H.L. He, Q. Wang, L. Liu, N.B. Luo, D.K. Su, G.Q. Jin, Peritumoral edema in preoperative magnetic resonance imaging is an independent prognostic factor for hepatocellular carcinoma, Clin. Imaging 75 (2021) 143–149, https://doi.org/10.1016/j.clinimag.2021.01.022.

[8] M. Rodriguez-Peralvarez, T.V. Luong, L. Andreana, T. Meyer, A.P. Dhillon, A. K. Burroughs, A systematic review of microvascular invasion in hepatocellular carcinoma: diagnostic and prognostic variability, Ann. Surg. Oncol. 20 (2013) 325–339, https://doi.org/10.1245/s10434-012-2513-1.

[9] Y.Q. Yu, L. Wang, Y. Jin, J.L. Zhou, Y.H. Geng, X. Jin, X.X. Zhang, J.J. Yang, C. M. Qian, D.E. Zhou, et al., Identification of serologic biomarkers for predicting microvascular invasion in hepatocellular carcinoma, Oncotarget 7 (2016) 16362–16371, https://doi.org/10.18632/oncotarget.7649.

[10] H.T. Hu, Z. Wang, X.W. Huang, S.L. Chen, X. Zheng, S.M. Ruan, X.Y. Xie, M.D. Lu, J. Yu, J. Tian, et al., Ultrasound-based radiomics score: a potential biomarker for the prediction of microvascular invasion in hepatocellular carcinoma, Eur. Radio. 29 (2019) 2890–2901, https://doi.org/10.1007/s00330-018-5797-0.

[11] W.M. Cong, H. Bu, J. Chen, H. Dong, Y.Y. Zhu, L.H. Feng, J. Chen, Practice guidelines for the pathological diagnosis of primary liver cancer: 2015 update, World J. Gastroenterol. 22 (2016) 9279–9287, https://doi.org/10.3748/wjg.v22.i42.9279.

[12] M. Kudo, Breakthrough Imaging in Hepatocellular Carcinoma, Liver Cancer 5 (2016) 47–54, https://doi.org/10.1159/000367761.

[13] F. Wang, K. Numata, H. Nihonmatsu, M. Okada, S. Maeda, Application of new ultrasound techniques for focal liver lesions, J. Med Ultrason 2020 (47) (2001) 215–237, https://doi.org/10.1007/s10396-019-01001-w.

[14] F. Zhu, F. Yang, J. Li, W. Chen, W. Yang, Incomplete tumor capsule on preoperative imaging reveals microvascular invasion in hepatocellular carcinoma: a systematic review and meta-analysis, Abdom. Radio. (NY) 44 (2019) 3049–3057, https://doi.org/10.1007/s00261-019-02126-9.

[15] L. Song, J. Li, Y. Luo, The importance of a nonsmooth tumor margin and incomplete tumor capsule in predicting HCC microvascular invasion on preoperative imaging examination: a systematic review and meta-analysis, Clin. Imaging 76 (2021) 77–82, https://doi.org/10.1016/j.clinimag.2020.11.057.

[16] J. Bo, F. Xiang, F. XiaoWei, Z. LianHua, L. ShiChun, L. YuKun, A nomogram based on contrast-enhanced ultrasound to predict the microvascular invasion in hepatocellular carcinoma, Ultrasound Med Biol. 49 (2023) 1561–1568, https://doi.org/10.1016/j.ultrasmedbio.2023.02.020.

[17] X. Zhong, J. Peng, Y. Xie, Y. Shi, H. Long, L. Su, Y. Duan, X. Xie, M. Lin, A nomogram based on multi-modal ultrasound for prediction of microvascular invasion and recurrence of hepatocellular carcinoma, Eur. J. Radiol. 151 (2022) 110281, https://doi.org/10.1016/j.ejrad.2022.110281.

[18] F. Wang, K. Numata, M. Chuma, H. Miwa, S. Moriya, K. Ogushi, M. Okada, M. Otani, Y. Inayama, S. Maeda, A study on the inconsistency of arterial phase hypervascularity detection between contrast-enhanced ultrasound using sonazoid and gadolinium-ethoxybenzyl-diethylenetriamine penta-acetic acid magnetic resonance imaging of hepatocellular carcinoma lesions, J. Med Ultrason 2021 (48) (2001) 215–224, https://doi.org/10.1007/s10396-021-01086-2.

[19] R. Zheng, X. Zhang, B. Liu, Y. Zhang, H. Shen, X. Xie, S. Li, G. Huang, Comparison of non-radiomics imaging features and radiomics models based on contrast-

enhanced ultrasound and Gd-EOB-DTPA-enhanced MRI for predicting microvascular invasion in hepatocellular carcinoma within 5 cm, Eur. Radio. 33 (2023) 6462–6472, https://doi.org/10.1007/s00330-023-09789-5.

[20] S.Y. Park, Nomogram: An analogue tool to deliver digital knowledge, J. Thorac. Cardiovasc Surg. 155 (2018) 1793, https://doi.org/10.1016/j.jtcvs.2017.12.107.

[21] M. Omata, A.L. Cheng, N. Kokudo, M. Kudo, J.M. Lee, J. Jia, R. Tateishi, K.H. Han, Y.K. Chawla, S. Shiina, et al., Asia-Pacific clinical practice guidelines on the management of hepatocellular carcinoma: a 2017 update, Hepatol. Int 11 (2017) 317–370, https://doi.org/10.1007/s12072-017-9799-9.

[22] A. Lyshchik, Y. Kono, C.F. Dietrich, H.J. Jang, T.K. Kim, F. Piscaglia, A. Vezeridis, J.K. Willmann, S.R. Wilson, Contrast-enhanced ultrasound of the liver: technical and lexicon recommendations from the ACR CEUS LI-RADS working group, Abdom. Radio. (NY) 43 (2018) 861–879, https://doi.org/10.1007/s00261-017-1392-0.

[23] A. Herrero, L. Boivineau, G. Cassese, E. Assenat, B. Riviere, S. Faure, J.U. Bedoya, F. Panaro, B. Guiu, F. Navarro, et al., Progression of AFP SCORE is a preoperative predictive factor of microvascular invasion in selected patients meeting liver transplantation criteria for hepatocellular carcinoma, Transpl. Int 35 (2022) 10412, https://doi.org/10.3389/ti.2022.10412.

[24] C. Zhang, R. Zhao, F. Chen, Y. Zhu, L. Chen, Preoperative prediction of microvascular invasion in non-metastatic hepatocellular carcinoma based on nomogram analysis, Transl. Oncol. 14 (2021) 100875, https://doi.org/10.1016/j.tranon.2020.100875.

[25] K. Huang, Z. Dong, H. Cai, M. Huang, Z. Peng, L. Xu, Y. Jia, C. Song, Z.P. Li, S. T. Feng, Imaging biomarkers for well and moderate hepatocellular carcinoma: preoperative magnetic resonance image and histopathological correlation, Bmc Cancer 19 (2019) 364, https://doi.org/10.1186/s12885-019-5574-8.

[26] Y. Zhu, B. Feng, W. Cai, B. Wang, X. Meng, S. Wang, X. Ma, X. Zhao, Prediction of Microvascular Invasion in Solitary AFP-Negative Hepatocellular Carcinoma $\leq$ 5 cm Using a Combination of Imaging Features and Quantitative Dual-Layer Spectral-Detector CT Parameters, Acad. Radio. 30 (Suppl 1) (2023) S104–S116, https://doi.org/10.1016/j.acra.2023.02.015.

[27] E.S. Cho, J.Y. Choi, MRI features of hepatocellular carcinoma related to biologic behavior, Korean J. Radio. 16 (2015) 449–464, https://doi.org/10.3348/kjr.2015.16.3.449.

[28] S. Lee, S.H. Kim, J.E. Lee, D.H. Sinn, C.K. Park, Preoperative gadoxetic acid-enhanced MRI for predicting microvascular invasion in patients with single hepatocellular carcinoma, J. Hepatol. 67 (2017) 526–534, https://doi.org/10.1016/j.jhep.2017.04.024.

[29] P.K. Bhattacharjee, A. Saito, M. Chiba, H. Katsuragawa, K. Takasaki, Detection of hepatocellular carcinoma capsule by contrast-enhanced ultrasound using Levovist: correlations with pathological findings, J. Med Ultrason 2005 (32) (2001) 167–172, https://doi.org/10.1007/s10396-005-0069-4.

[30] T. Nakashima, M. Kojiro, T. Nakashima, M. Kojiro, Histological growth patterns of hepatocellular carcinoma, Hepatocell. Carcinoma.: Atlas Its Pathol. (1987) 81–104.

[31] Y. Deng, D. Yang, H. Xu, A. Ren, Z. Yang, Diagnostic performance of imaging features in the HBP of gadoxetate disodium-enhanced MRI for microvascular invasion in hepatocellular carcinoma: a meta-analysis, Acta Radio. 63 (2022) 1303–1314, https://doi.org/10.1177/02841851211038806.

[32] S. Wang, W. Zheng, Z. Zhang, G.H. Zhang, D.J. Huang, Microvascular invasion risk scores affect the estimation of early recurrence after resection in patients with hepatocellular carcinoma: a retrospective study, Bmc Med Imaging 22 (2022) 204, https://doi.org/10.1186/s12880-022-00940-0.

[33] N.R. Kim, H. Bae, H.S. Hwang, D.H. Han, K.S. Kim, J.S. Choi, M. Park, G.H. Choi, Preoperative Prediction of Microvascular Invasion with Gadoxetic Acid-Enhanced Magnetic Resonance Imaging in Patients with Single Hepatocellular Carcinoma: The Implication of Surgical Decision on the Extent of Liver Resection, Liver Cancer (2023) 1–12, https://doi.org/10.1159/000531786.

[34] J. Chen, J. Zhou, S. Kuang, Y. Zhang, S. Xie, B. He, Y. Deng, H. Yang, Q. Shan, J. Wu, et al., Liver imaging reporting and data system category 5: MRI predictors of microvascular invasion and recurrence after hepatectomy for hepatocellular carcinoma, AJR Am. J. Roentgenol. 213 (2019) 821–830, https://doi.org/10.2214/AJR.19.21168.

[35] H. Wei, H. Jiang, X. Liu, Y. Qin, T. Zheng, S. Liu, X. Zhang, B. Song, Can LI-RADS imaging features at gadoxetic acid-enhanced MRI predict aggressive features on pathology of single hepatocellular carcinoma, Eur. J. Radio. 132 (2020) 109312, https://doi.org/10.1016/j.ejrad.2020.109312.

[36] J.Y. Huang, Z.L. Huang, Z. Yang, X.P. Zheng, Contrast-enhanced ultrasound predicts microvascular invasion in patients with hepatocellular carcinoma, Hepatobiliary Pancreat. Dis. Int 21 (2022) 609–613, https://doi.org/10.1016/j.hbpd.2022.05.008.

[37] P. Wang, F. Nie, T. Dong, G. Wang, L. Wang, X. Fan, Study on correlation between two-dimensional ultrasound, contrast-enhanced ultrasound and microvascular invasion in hepatocellular carcinoma, Clin. Hemorheol. Micro 80 (2022) 97–106, https://doi.org/10.3233/CH-211190.

[38] C. Tian, L. Li, L. Fan, A. Brown, E.J. Norris, M. Morrison, E.S. Glazer, L. Zhu, A hepatoprotective role of peritumoral non-parenchymal cells in early liver tumorigenesis, Dis. Model Mech. (2023) 16, https://doi.org/10.1242/dmm.049750.

[39] Y. Tian, H. Hua, Q. Peng, Z. Zhang, X. Wang, J. Han, W. Ma, J. Chen, Preoperative Evaluation of Gd-EOB-DTPA-Enhanced MRI Radiomics-Based Nomogram in Small Solitary Hepatocellular Carcinoma ($\leq$3 cm) With Microvascular Invasion: A Two-Center Study, J. Magn. Reson Imaging 56 (2022) 1459–1472, https://doi.org/10.1002/jmri.28157.

[40] H.Q. Gu, C. Liu, Clinical prediction models: evaluation matters, Ann. Transl. Med 8 (2020) 72, https://doi.org/10.21037/atm.2019.11.143.

[41] D.G. Altman, P. Royston, The cost of dichotomising continuous variables, BMJ 332 (2006) 1080, https://doi.org/10.1136/bmj.332.7549.1080.